Nano-Micro Letters

e-ISSN 2150-5551
CN 31-2103/TB

ARTICLE

https://doi.org/10.1007/s40820-022-00992-5

Cite as
Nano-Micro Lett.
(2023) 15:17

Received: 16 October 2022
Accepted: 5 December 2022
Published online: 29 December 2022

Stabilizing Buried Interface via Synergistic Effect of Fluorine and Sulfonyl Functional Groups Toward Efficient and Stable Perovskite Solar Cells

Cheng Gong[1], Cong Zhang[1], Qixin Zhuang[1], Haiyun Li[1], Hua Yang[2], Jiangzhao Chen[1] ✉, Zhigang Zang[1] ✉

HIGHLIGHTS

- An effective buried interface stabilization strategy based on synergistic effect of fluorine and sulfonyl functional groups is proposed.
- The correlations between molecular structures, defect passivation, interfacial energy band alignment, perovskite crystallization and device performance are established.
- The device with KFSI achieves an impressive efficiency of 24.17%.

ABSTRACT The interfacial defects and energy barrier are main reasons for interfacial nonradiative recombination. In addition, poor perovskite crystallization and incomplete conversion of PbI_2 to perovskite restrict further enhancement of the photovoltaic performance of the devices using sequential deposition. Herein, a buried interface stabilization strategy that relies on the synergy of fluorine (F) and sulfonyl (S=O) functional groups is proposed. A series of potassium salts containing halide and non-halogen anions are employed to modify SnO_2/perovskite buried interface. Multiple chemical bonds including hydrogen bond, coordination bond and ionic bond are realized, which strengthens interfacial contact and defect passivation effect. The chemical interaction between modification molecules and perovskite along with SnO_2 heightens incessantly as the number of S=O and F augments. The chemical interaction strength between modifiers and perovskite as well as SnO_2 gradually increases with the increase in the number of S=O and F. The defect passivation effect is positively correlated with the chemical interaction strength. The crystallization kinetics is regulated through the compromise between chemical interaction strength and wettability of substrates. Compared with Cl^-, all non-halogen anions perform better in crystallization optimization, energy band regulation and defect passivation. The device with potassium bis (fluorosulfonyl) imide achieves a tempting efficiency of 24.17%.

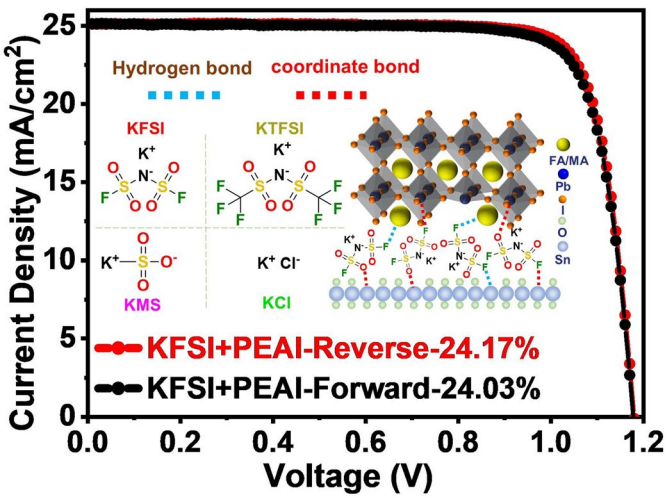

KEYWORDS Perovskite solar cells; Buried interface; Multiple chemical bonds; Synergistic effect of functional groups; Defect passivation

✉ Jiangzhao Chen, jiangzhaochen@cqu.edu.cn; Zhigang Zang, zangzg@cqu.edu.cn
[1] Key Laboratory of Optoelectronic Technology and Systems (Ministry of Education), Chongqing University, Chongqing 400044, People's Republic of China
[2] Institute of High Energy Physics, Chinese Academy of Sciences (CAS), Beijing 100049, People's Republic of China

1 Introduction

These merits including low cost, solution processing and outstanding power conversion efficiency (PCE) make perovskite solar cells (PSCs) attract mammoth attention in academia and industry [1–5]. The superior properties of perovskites should be responsible for the extremely rapid PCE increase from 3.8% in 2009 [6] to presently certified 25.7% [7]. However, the further performance improvement is severely limited by the interfacial nonradiative recombination [8]. In regular PSCs, the interface of electron transport layer (ETL) with perovskite layer is usually referred to as buried interface. It is very difficult to perform in situ characterization of the bottom surface of perovskite films [9]. Therefore, it is much more challenging to modify buried interface compared with the perovskite/hole transport layer (HTL) interface. Buried interfacial defects are a main reason of interfacial non-radiative recombination [10]. The charge trap density at grain boundary (GB) and interface was reported to be much larger than that within perovskite grains [11]. Moreover, the donor type defects and acceptor type defects may exist simultaneously at buried interface which are usually deep-level defects [12, 13]. It is well known that considerable quantity of Sn interstitial defects (Sn_i) and oxygen vacancy defects (V_o) usually distribute at the surface and in the interior of SnO_2 ETL [14]. Sn_i and V_o defects can be formed spontaneously because of their low formation energies which can affect the photoelectric properties and energy levels of SnO_2 [15]. The trap carriers at the heterojunction interface are easy to be trapped by interfacial deep-level defects, resulting in interfacial non-radiative recombination losses and accordingly diminishing PCE and stability. Apart from buried interface defects, interfacial energy barrier resulting from imperfect energy band alignment also could result in interfacial carrier nonradiative recombination [8]. Interface modification by appropriate materials can improve interfacial energy band alignment and minimize interfacial energy barrier, resulting in enhanced device performance [12, 16, 17]. The quality of perovskite films plays a key role in fabricating stable and efficient PSCs. The perovskite film quality is primarily determined by its crystallization process. One step and two step approaches are usually employed to prepare perovskite films. Nevertheless, the PCEs of the PSCs based on two step method [18–20] are still lower than that of the PSCs using one step method [4, 21]. This should be due to more difficult crystallization control for two step method as compared to one step method. It has been extensively demonstrated that it is an effective approach to modulate perovskite crystallization by modifying ETL substrates [22, 23]. In a word, multifunctional molecules are urgently needed to be developed to manage interfacial carrier through simultaneous realization of interfacial defects passivation, interfacial energy band alignment optimization and perovskite crystallization modulation.

To date, huge efforts have been devoted to developing various materials to modify buried interface. However, reported most interface molecules have relatively simple functions, either passivating defects, tuning interfacial energy band alignment or modulating perovskite crystallization [24–26]. It is of great importance for simultaneously achieving multiple functions to enrich chemical bonding modes (e.g., ionic bond, coordination bond and hydrogen bond). Among various interface materials, salts containing both cation and anion are the most appropriate candidate for realizing multiple chemical bonds with perovskite and SnO_2 layers [16, 17, 27, 28]. The anions and cations in salts can form ionic bonds with charged defects in perovskite films and thus passivate simultaneously positively and negatively charged defects. Fluorine functional groups incorporating into cations and/or anions can not only form hydrogen bond with organic cations in perovskites but also form coordination bond with Pb^{2+} and Sn^{4+} [17, 28]. This suggests that fluorination strategy is a feasible and effective approach to accomplish multiple functions induced by multiple chemical bonds. Except for fluorination strategy, introduction of functional groups (e.g., C=O [29, 30], S=O [16], and C=S [31, 32]) in cation and anion is another effective method for enriching chemical interaction modes because these ligand functional groups can effectively passivate defects and control crystallization kinetics. In recent several years, the additive or interface molecules containing non-halogen anions have received considerable attention [33], Non-halogen anions play an important role in defect passivation ($HCOO^-$, CO_3^{2-}, PO_4^{3-} and NO_3^-) [34–37], crystallization regulation ($HCOO^-$, SCN^- and SO_4^{2-}) [2, 37–41], and energy level alignment modulation (BF_4^- and PF_6^-) [17, 28, 42]. However, compared with halide anions, the working mechanism of non-halogen anions is still obscure. In addition, the synergistic effect of non-halogen and halogen functional groups in same anions is still not revealed up to now. Here, it needs to

 https://doi.org/10.1007/s40820-022-00992-5

be noted that most researches often adopted single non-halogen anion to modify buried interface [28, 39]. For example, the use of a single non-halogen anion to improve crystallinity and interfacial carrier transport in perovskite films has been reported by Singh et al. and Chen et al. [43, 44]. The specific roles of various functional groups contained in non-halogen anions and the laws of their synergistic effects have not yet been revealed. At the same time, it is difficult for non-halogen anions to be used at the perovskite/HTL interface to exert their maximum potential, because the modified molecules can only interact with the perovskite film and not with the HTL layer. However, this is not beneficial for maximizing the potentials of non-halogen anions. Therefore, it is urgently needed to systematically and deeply uncover the relationships between structures of non-halogen anions, properties of non-halogen anions, defect density, interfacial carrier dynamics and device performance.

In this work, we proposed a buried interface stabilization strategy based on synergistic engineering of fluorine and sulfonyl functional groups, which enhanced the PCE and stability of planar PSCs using two step method. Potassium chloride (KCl, reference molecule), potassium methanesulfonyl (KMS), potassium bis (fluorosulfonyl) imide (KFSI) and potassium bis (trifluoromethanesulfonyl) imide (KTFSI) were used to modulate buried interface. S=O functional group and non-halogen anion can form coordination bond with Pb^{2+} and Sn^{4+}. K^+ and non-halogen anions can form ionic bonds with cation and halide vacancy defects, respectively. In short, multiple chemical bonds between modifiers and functional layers were achieved. The defect passivation effect was determined by chemical interaction strength. For energy band modulation, appropriate number of S=O and F functional groups was required. In case of crystallization control, the compromise between chemical interaction strength and wettability of substrates should be considered simultaneously. The introduction of F would enhance chemical interaction while it also would increase hydrophobicity of surface of ETL. Appropriate hydrophobicity is conducive to inhibiting heterogeneous nucleation and thus facilitating perovskite crystallization but too high hydrophobicity hinders perovskite crystallization. Taken together, KFSI is the best in increasing device performance. Compared with Cl^-, all non-halogen anions exhibited better passivation effect, energy band alignment and perovskite crystallization, which highlights importance of non-halogen anions in interface engineering. The KFSI-modified device delivered a promising PCE of 24.17% along with excellent stability. This work demonstrated superiority of non-halogen anions and provide a guidance for enhancing photovoltaic performance of PSCs by managing interfacial carrier via the synergistic design of organic functional groups.

2 Experimental Section

2.1 Materials

The tin (IV) oxide (SnO_2, 15% in H_2O colloidal dispersion) was bought from Alfa Aesar. Lead (II) iodide (PbI_2, 99.99%), Spiro-OMeTAD (99.86%), formamidine hydroiodide (FAI, 99.5%), methylammonium iodide (MAI, 99.9%), and methylamine hydrochloride (MACl, 99.9%) were bought from Advanced Election Technology Co., Ltd. N, N-dimethylformamide (DMF, 99.8%), 2-propanol (IPA, 99.9%), dimethyl sulfoxide (DMSO, 99.9%), chlorobenzene (CB, 99.8%), and acetonitrile (ACN, 99.8%) were obtained from Sigma-Aldrich. Bis(trifluoromethane) sulfonimide lithium salt (Li-TFSI, 99%) and 4-tertbutylpyridine (tBP, 99%) were obtained from Xi'an Polymer Light Technology Corp. Potassium chloride (KCl, 99.8%), potassium methanesulfonate (KMS, 98.0%), potassium bis (trifluoromethanesulfonyl) imide (KTFSI, 97%), potassium bis (fluorosulfonyl) imide (KFSI, 97%) were purchased from Aladdin.

2.2 Device Fabrication

The etched ITO glass was ultrasonically cleaned sequentially by detergent, deionized water, ethanol, acetone and IPA. The SnO_2 colloidal solution was spin-coated on the ITO substrates at 4000 rpm for 30 s and then the SnO_2-coated ITO substrates were annealed at 150 °C for 30 min. Afterwards, SnO_2 films were treated by UV-ozone for 15 min. For modified SnO_2 films, different concentrations of KCl solution in water, KMS solution in IPA, KTFSI solution in IPA and KFSI solution in IPA were spin-coated onto the SnO_2 films at 5000 rpm for 30 s and annealed at 100 °C for 5 min. The PbI_2 solution (691.5 mg, 1.5 mmol mL^{-1}) in DMF:DMSO (9:1) was spin-coated onto pristine and modified SnO_2 films at 1500 rpm for 30 s and then PbI_2 films were annealed at 68 °C for 1 min. After the PbI_2 film cooled down to room temperature, 45 µL of organic mixture solution of FAI (90 mg), MAI (6.39 mg) and MACl (9 mg) in 1 mL IPA

was spin-coated onto PbI_2 films at 2300 rpm for 30 s, and then the films were transferred to ambient air condition (30–40% humidity) and annealed at 150 °C for 15 min. For PEAI modified perovskite films, the 2 mg mL^{-1} of PEAI solution in IPA was spin-coated onto the perovskite films at 5000 rpm for 30 s without annealing. The hole transport material solution was prepared through dissolving 72.3 mg Spiro-OMeTAD, 35 µL Li-TFSI stock solution (260 mg Li-TFSI in 1 mL acetonitrile), and 30 µL tBP in 1 mL CB. Then the hole transport layer (HTL) was prepared by spin-coating a Spiro-OMeTAD solution on the top of the perovskite layer at 4000 rpm for 30 s. Finally, 100 nm of Ag electrode was thermally evaporated on HTL using a shadow mask.

2.3 Film Characterization

The field emission scanning electron microscopy (FE-SEM, JEOL JSM-7800F) was applied to characterize cross-sectional and surface morphology of perovskite films. X-ray diffraction (XRD) patterns were acquired using a PANalytical Empyrean diffractometer equipped with Cu Kα radiation ($\lambda = 1.5406$ Å). X-ray photoelectron spectroscopy (XPS) and ultraviolet photoelectron spectroscopy (UPS) were measured by Thermo Fisher Escalab 250Xi spectrometer using a monochromatized Al source. XPS was calibrated using the peak position of C 1*s* and UPS was calibrated using the work function of Au. In particular, the samples tested for XPS measurements were prepared by spin-coating the perovskite precursor solutions with different modifiers and annealed to form perovskite films. The optical absorption and transmission spectra were measured by Shimadzu UV3600 Spectrophotometer. The steady-state and time-resolved photoluminescence spectra were performed with a fluorescence spectrophotometer (FLS1000, Edinburgh Instruments Ltd.) which was equipped with a pulse laser diode with a wavelength of 450 nm. The conductivity of SnO_2 were carried out on Keithley 2400 source meter with a structure of ITO/PCBM/SnO_2 without or with KCl, KMS, KFSI and KTFSI/perovskite/PCBM/Ag. Two-dimensional grazing-incidence wide-angle X-ray scattering (GIWAXS) images were collected on BL1W1A at the Beijing Synchrotron Radiation Facility (BSRF) ($\lambda = 1.54$ Å). The trap state density (n_t) was determined by the onset of the trap filling limit voltage (V_{TFL}) according to Eq. (1) [45]:

$$V_{TFL} = (en_tL^2)/(2\varepsilon_0\varepsilon_r) \quad (1)$$

where ε_0 is the permittivity of free space, ε_r is the relative permittivity of perovskite, e denotes the elementary charge and L is the thickness of perovskite layer. Space charge limited current (SCLC) measurement was applied to determine the electron trap density and mobility using the electron-only device with a structure of ITO/SnO_2/(KCl, KMS, KFSI or KTFSI)/PCBM/Ag. The SCLC method was employed to measure the electron mobility of the pristine SnO_2 film and modified SnO_2 films. The electron mobility (μ_e) is calculated by Eq. (2) [46]:

$$\mu_e = \frac{8JL^3}{9\varepsilon\varepsilon_0(V_{app} - V_{bi})^2} \quad (2)$$

where J is the current density, L is the thickness of ETL, ε is the relative dielectric constant of ETL, ε_0 is the vacuum permittivity, V_{app} is the applied voltage, and V_{bi} is the built-in voltage due to the different work function of the two electrodes. The Fourier transforms infrared (FTIR) spectra were recorded by Nicolet iS50 Infrared Fourier transform microscope (Thermo Fisher Scientific) in the transmittance mode. The samples with a structure of ITO/SnO_2/without or with KCl, KMS, KFSI or KTFSI/perovskite film were prepared for FTIR measurements. The texture coefficient (*TC*) of the specified plane is determined from the XRD spectra and calculated by Eq. (3) [47],

$$TC(hkl) = \left\{\frac{I_m(hkl)}{I_0(hkl)}\right\}\left\{\frac{1}{n}\sum_1^n \frac{I_m(hkl)}{I_0(hkl)}\right\}^{-1} \quad (3)$$

where $I_m(hkl)$ is intensity of the (hkl) diffraction peak on the sample under investigation, $I_0(hkl)$ is the intensity of the (hkl) plane from a powder diffraction file, and n is the number of diffractions considered in the analysis. The powder diffraction profiles of $FAPbI_3$ for reference were taken from the report of Stoumpos et al. [48].

2.4 Device Characterization

The current density–voltage (*J-V*) characteristics of the devices were measured in ambient air (the relative humidity was 40%–50%) by a solar simulator equipped with 450 W Xenon lamp (Newport, 2612A) and a Keithley 2400 source meter. Light intensity was adjusted to AM 1.5G one sun (100 mW cm^{-2}) with a NIM calibrated standard Si solar cell. A metal mask with an aperture area of 0.04 cm^2 was applied on top of the cell to define active area. The incident photon-to-current efficiency (IPCE) measurement was performed

 https://doi.org/10.1007/s40820-022-00992-5

on a Newport Instruments system (Newport-74125) coupled with a lock-in amplifier and a 300 W Xenon lamp. Transient photocurrent (TPC) and transient photovoltage (TPV) measurements were performed using a system excited by a 532 nm (1000 Hz, 6 ns) pulsed laser. Recording photocurrent or photovoltage decay process used a 1 GHz Agilent digital oscilloscope (DSO-X3102A) with a 50 X or 1 MX sampling resistor. The device stacks used to measure TPC and TPV are complete device, which includes the substrate ITO, electron and hole transport layer, and silver electrode.

3 Results and Discussion

3.1 Chemical Interaction Mechanisms Investigation

Figure 1a shows the molecular structures of KCl, KMS, KFSI and KTFSI. It is schematically illustrated that modification molecules could bridge perovskite and SnO_2 films by rich chemical bonds. The chemical interactions between modifier and perovskites or ETL were investigated by XPS and FTIR spectroscopy measurements. In Fig. 1b, the

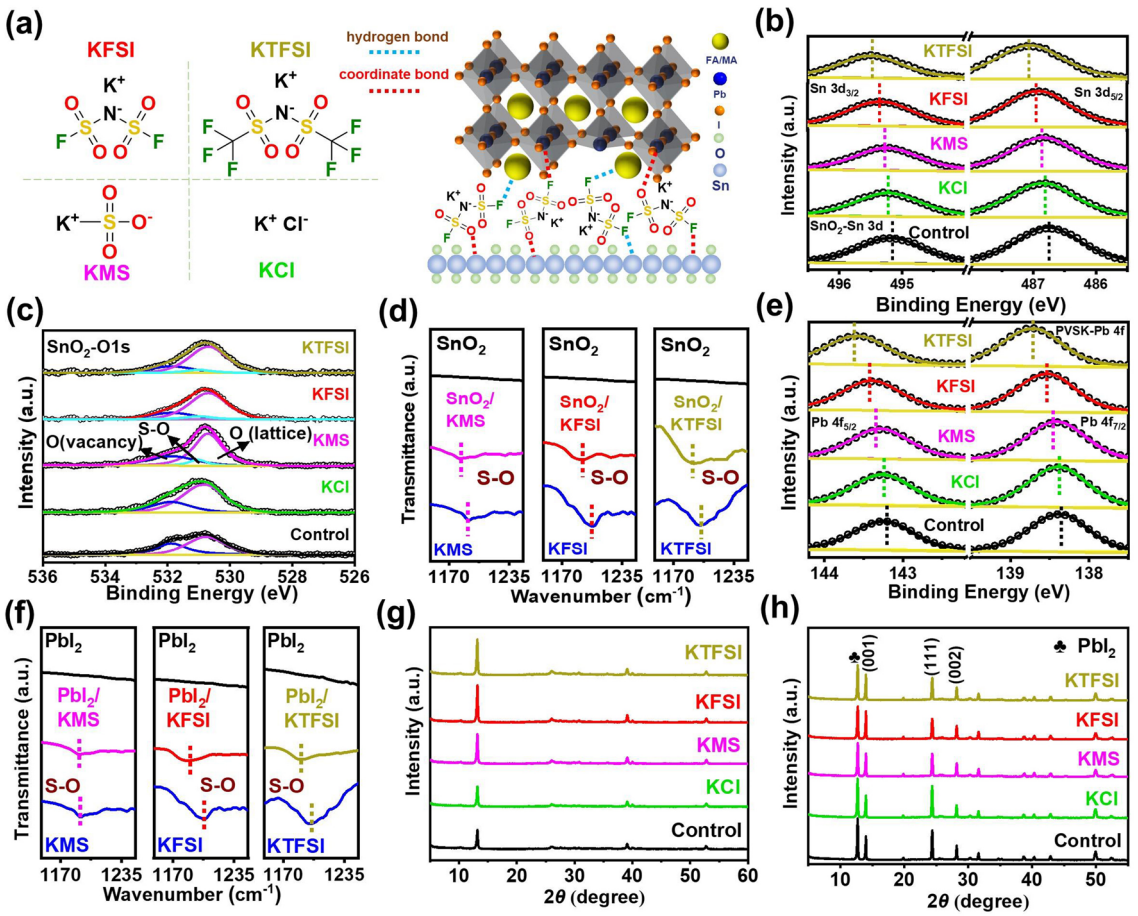

Fig. 1 **a** Molecular structures of potassium salts used for modifying buried interface and schematic illustration of the interaction of modifiers and functional layers. **b** Sn 3d and **c** O 1*s* XPS spectra of the control and modified SnO_2 layers. **d** FTIR spectra of pure KMS, KTFSI and KFSI and the SnO_2 films without and with KMS, KTFSI and KFSI. **e** XPS spectra of the control and modified perovskite films. **f** FTIR spectra of the PbI_2 films with or without KMS, KTFSI and KFSI. XRD patterns of the **g** PbI_2 films and **h** perovskite films deposited on SnO_2 ETLs without or with KCl, KMS, KTFSI and KFSI

binding energies of Sn $3d_{5/2}$ and Sn $3d_{3/2}$ of the pristine SnO_2 layer were increased inch by inch in the order of KCl, KMS, KFSI and KTFSI. Among them, the sample modified by KTFSI had the largest binding energy shift, which indicates that the interaction of modifiers with ETL is positively correlated with the quantity of F and S=O. It is found from Fig. 1c that O 1*s* peak can be divided into two peaks. One is lattice oxygen (O_L) and the other is vacancy oxygen (O_V) [12, 28]. The KMS, KFSI and KTFSI-modified SnO_2 had a characteristic peak of S–O, and the enlarged view is shown in Fig. S1. The peak area ratios of O_V to O_L were calculated to be 0.66, 0.65, 0.42, 0.38 and 0.29 for bare, KCl, KMS, KFSI and KTFSI modified SnO_2, respectively. This shows that passivation effect of anions for oxygen vacancy defects gradually improved with the increase in chemical interaction strength. SnO_2-KTFSI had the smallest oxygen vacancy density, suggesting that the incorporation of strongly coordinated F and S=O functional groups is favorable for defect passivation. In Fig. S2, the Sn–O peak in bare SnO_2 sample was at 695 cm^{-1}, which was moved to 698, 705, 709 and 714 cm^{-1} for KCl, KMS, KFSI and KTFSI treated SnO_2, respectively. This indicates that all anions can interact with SnO_2 but stronger interaction was found for non-halogen anions than Cl^-, which could be presence of F and S=O in non-halogen anions. Interestingly, a new peak attributed to Sn-F bond appeared in SnO_2-KTFSI and SnO_2-KFSI, implying that F in FSI^- and $TFSI^-$ can coordinate with undercoordinated Sn^{4+} [17, 28]. In Fig. 1d, the peaks around 1191.1, 1203.9 and 1198.1 cm^{-1} belonging to S=O stretching vibration in pure KMS, KFSI and KTFSI, respectively, whereas the peaks were shifted to 1185.4, 1195.6 and 1186.6 eV for KMS, KFSI and KTFSI modified SnO_2 films, respectively, which confirmed the interaction between S=O and undercoordinated Sn^{4+} and/or oxygen vacancies. Likewise, peak shift degree gradually increased in the order of KMS, KFSI and KTFSI. Figure 1e reveals that the binding energies of Pb $4f_{5/2}$ and Pb $4f_{7/2}$ were gradually increased from the control film (143.24 and 138.26 eV), the perovskite film with KCl (143.26 and 138.38 eV), the perovskite film with KMS (143.29 and 138.41 eV), the perovskite film with KFSI (143.40 and 138.52 eV) to the perovskite film with KTFSI (143.58 and 138.70 eV), which should be due to interaction of Pb^{2+} with S=O and/or F. Moreover, the S–O peak shift also revealed the interaction between S=O and Pb^{2+} (Fig. 1f). We found in Fig. S3 that N–H peak was not shifted for KCl and KMS modified perovskite films with respect to the control film while the peak shift degree gradually increased from KFSI to KTFSI, which is indicative of gradually enhanced hydrogen bond strength with the increase in the number of F functional group. N 1*s* XPS spectra in Fig. S4 and FTIR spectra in Fig. S5 also certified the above change tendency of hydrogen bond strength. In conclusion, we have demonstrated that anions in modifiers can chemically interact with both ETL and perovskites and chemically link the two important functional layers. Furthermore, it was uncovered that F and S=O in non-halogen anions can interact with both functional layers. The strong chemical interaction should contribute to improved interfacial contact and thus enhancing PCE and stability.

Figures S6 and S7 demonstrate that light transmittance and bandgap of SnO_2 almost did not change after the modification of different potassium salts. After modification, the conductivity and electron mobility of ETL was slightly increased (Figs. S8 and S9), which is attributed to effective passivation of these modifiers for oxygen vacancy and undercoordinated Sn^{4+} defects [49]. The UPS test was performed to calculate energy band values of the control and modified ETLs (Fig. S10). It is seen from Fig. S11 and Table S1 that the conduction band minimum (CBM) and valence band maximum (VBM) were gradually upshifted in the order of bare SnO_2, SnO_2-KCl, SnO_2-KMS, SnO_2-KTFSI and SnO_2-KFSI. The introduction of highly electronegative F and S = O in non-halogen anions accounts for upshifted CBM and VBM. Improved interfacial energy band alignment should promote electron extraction and transfer, which leads to inhibiting interfacial nonradiative recombination and increasing photovoltaic parameters.

3.2 Crystallization and Morphology of Perovskite Films

XRD measurement was performed to study the crystal structure and crystallinity of the PbI_2 and perovskite films without and with KCl, KMS, KFSI and KTFSI. As presented in Fig. 1g, the characteristic diffraction peak intensity of PbI_2 was gradually increased from pristine PbI_2, PbI_2-KCl, PbI_2-KMS, PbI_2-KTFSI to PbI_2-KFSI, suggesting that these modifiers can accelerate the crystallization of PbI_2 films. From Fig. 1h, the same change trend was observed for the perovskite films. The peak intensity of PbI_2 gradually reduced and the intensity of (001) crystal plane from

 https://doi.org/10.1007/s40820-022-00992-5

perovskites gradually increased in the order of the control perovskite, perovskite with KCl, perovskite with KMS, perovskite with KTFSI and perovskite with KFSI. The gradually enhanced *TC* in Table S2 and Fig. S12 indicates that the perovskite grew along (001) crystal plane after interface modification and the orientation growth was gradually enhanced in the order of KCl, KMS, KTFSI and KFSI-modified perovskite films. (001) crystal plane is perpendicular to the substrate and is can facilitate carrier transport and collection. The strong chemical interaction is beneficial for the crystallization of PbI_2 and perovskite films but superabundant F would increase contact angle and reduce wettability of ETL substrates (Fig. S13). It was reported that appropriate hydrophobicity is conducive to repressing heterogeneous nucleation and promoting perovskite homogeneous nucleation [49]. Consequently, the KFSI-modified perovskite film exhibited higher crystallinity compared with KTFSI-modified one. It shows that interfacial chemical interaction and wettability should be simultaneously considered when we design interface molecules.

The SEM images of pristine PbI_2 and PbI_2 films modified by KCl, KMS, KFSI or KTFSI are shown in Fig. S14. The KFSI-modified PbI_2 films show uniform and dense morphology, which could be beneficial to form smooth and highly crystalline perovskite layer [50]. As shown in Fig. S15, the bright rings at $q_{xy} = 0.9$ and 1.0 $Å^{-1}$ (where q_{xy} was the scattering vector, $q_{xy} = 4\pi \sin\theta/\lambda$) were the diffraction peaks for (001) crystal planes of PbI_2 and perovskite, respectively [51]. The diffraction spot of perovskite corresponding to (001) crystal plane became more and more discrete in the order of control, KCl-, KMS-, KTFSI- and KFSI-modified perovskite films. This suggests that the conversion of PbI_2 to perovskite was promoted and the perovskite crystallization was improved after interface medication. Moreover, non-halogen anions were more effective in modulating the crystallization in contrast to Cl^-. The synergistic effect of F and S=O functional groups play a key role in preparing superior perovskite layers. The SEM images of the perovskite films based on the bare and modified SnO_2 substrates are exhibited in Fig. 2a-b. The uniformity and compactness were improved after interface modification. The grain size was increased from 0.76 μm of the pristine perovskite film to 0.82, 0.93, 1.14 and 1.03 μm of the films modified by KCl, KMS, KFSI and KTFSI, respectively (Fig. S16). The enlarged grain size and ameliorated morphology are attributed to the improved crystallization. We can see from Fig. 2c that the cross section of the control perovskite film was composed of small perovskite grains while the large perovskite grain was across the whole cross section for modified perovskite films. Moreover, the KFSI modified perovskite film seems to show the best cross section, which is in good agreement with its highest crystallinity and best orientation revealed by XRD and GIWAXS results.

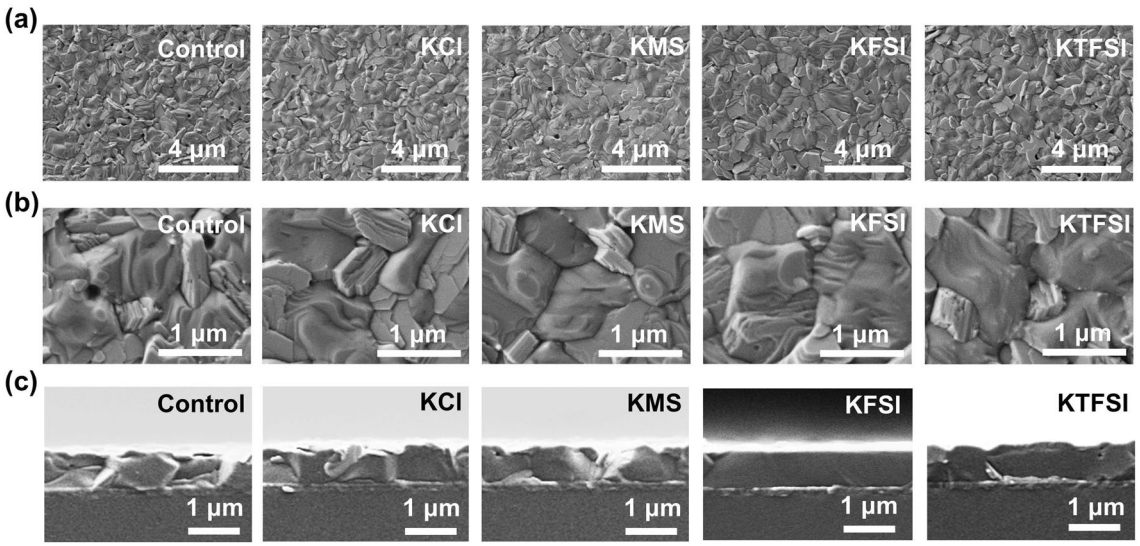

Fig. 2 **a, b** Top-view and **c** cross-sectional SEM images of the control and modified perovskite films

3.3 Carrier Lifetimes and Defect Densities of Perovskite Films

We investigated the light harvesting properties of the perovskite films without and with modifiers by performing ultraviolet–visible (UV–vis) absorption measurement. As exhibited in Fig. 3a, similar absorption properties were found for all perovskite films. All potassium salts modification can increase photoluminescence (PL) intensity regardless of measuring direction (perovskite or glass side). However, we observed the more significant PL intensity enhancement upon detecting from glass side as compared to perovskite side, indicating modifier could effectually cure buried interface (Fig. 3b-d). The time-resolved PL (TRPL) curves were fitted by the double exponential function Eq. (4):

$$I(t) = I_0 + A_1 e^{(-t/\tau_1)} + A_2 e^{(-t/\tau_2)} \quad (4)$$

where A_1 and A_2 represent the decay amplitude of fast and slow decay processes, respectively, τ_1 and τ_2 stand for the fast and slow decay time constants, respectively [28, 52]. The average carrier lifetime (τ_{ave}) is obtained through using Eq. (5):

$$\tau_{ave} = (A_1\tau_1^2 + A_2\tau_2^2)/(A_1\tau_1 + A_2\tau_2) \quad (5)$$

The corresponding fitting data are displayed in Table S3. The carrier lifetime change tendency from perovskite side is same as that from glass side but enhancement degree of the latter is much larger than that of the former, which agrees with steady state PL (SSPL) results. It was shown that non-halogen anions possessed better defect passivation effect relative to Cl^-. The strong chemical interaction is conducive to passivating defects but far too many F would remarkably increase the hydrophobicity of surface of ETLs and thus is not beneficial for perovskite crystallization. The reproducibility of the above PL results was affirmed by PL mapping images in Fig. 1f.

The trap density of the perovskite films without and with modifiers was quantified by the space charge limited current (SCLC) measurement in Fig. 3k. The perovskite film with KFSI possessed the least trap density of 6.08×10^{14} cm^{-3}, which was increased to 7.73×10^{14}, 9.39×10^{14}, 1.33×10^{15} and 1.55×10^{15} cm^{-3} for the KTFSI, KMS, KCl and control films, respectively. This suggests that the defect passivation effect increased in the order of KCl, KMS, KTFSI and KFSI.

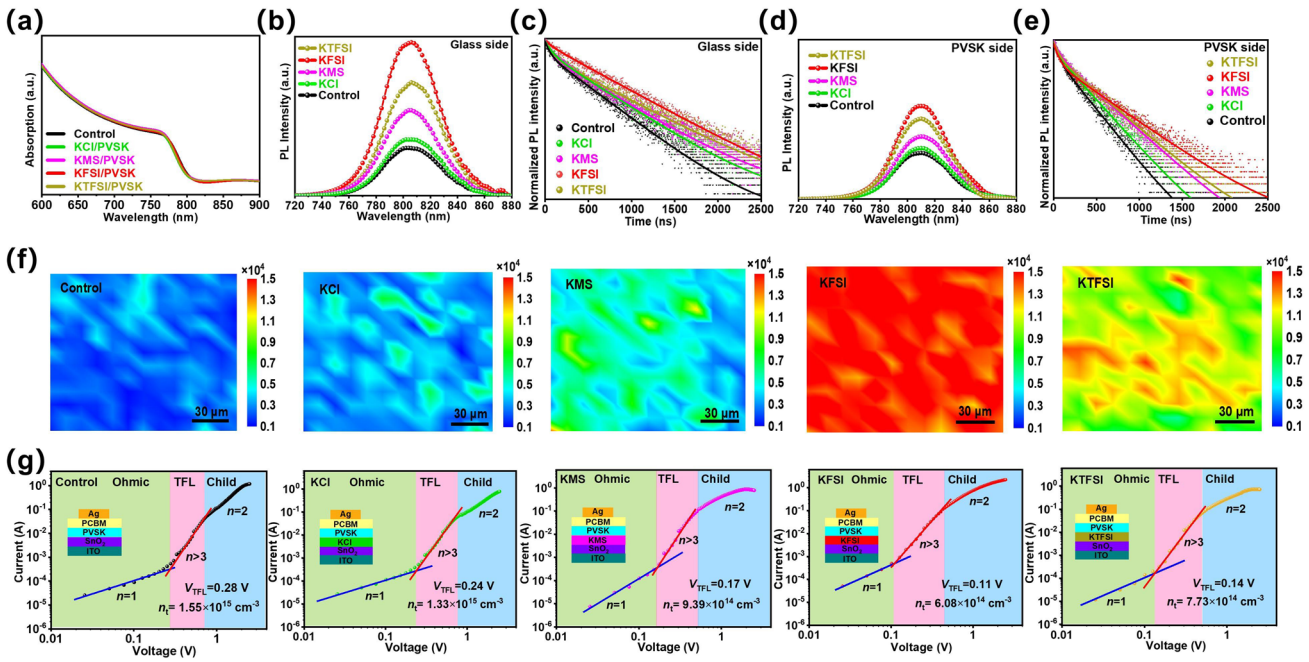

Fig. 3 **a** UV–vis absorption spectra of the perovskite films with or without modifiers. **b, d** SSPL and **c, e** TRPL spectra of the perovskite films prepared on non-conductive glass without and with modifiers by measuring from the **b, c** glass side or **d, e** perovskite side. **f** PL mapping images of the perovskite films deposited on non-conductive glass without and with modifiers. **g** Dark *I–V* curves of the electron-only devices

 https://doi.org/10.1007/s40820-022-00992-5

Reduced defect density and increased carrier lifetimes are ascribed to effective defect passivation and improved perovskite crystallization. Although KTFSI had the best defect passivation effect due to its strongest interaction with perovskite as well as ETL, KFSI had the smallest defect density and longest carrier lifetime, which is because of the trade-off between defect passivation effect and crystallization of PbI_2 and perovskite. It can be concluded that appropriate number of F is of great importance for simultaneously considering defect passivation and crystallization. The suppressed trap-assisted nonradiative recombination due to the decreased defect density and enhanced carrier lifetime should be main reason for enhanced open-circuit voltage (V_{OC}) and fill factor (FF).

3.4 Interfacial Carrier Dynamics Investigation

From Fig. 4a–b and Table S4, we observed gradually reduced PL intensities and carrier lifetimes in the order of SnO_2/perovskite, SnO_2/KCl/perovskite, SnO_2/KMS/perovskite, SnO_2/KTFSI/perovskite, and SnO_2/KFSI/perovskite, demonstrating gradually improved charge extraction, which is because of ameliorated energy band alignment and inhibited trap-mediated nonradiative recombination. The PL mappings also certified ameliorated charge extraction, as presented in Fig. 4c–g. In Fig. 4h, in contrast to the control device, the KCl, KMS, KTFSI and KFSI based devices demonstrated increased built-in potential (V_{bi}), which is suggestive of improved carrier separation and extraction due to more favorable band alignment. Subsequently, the transient photocurrent (TPC) decay in Fig. 4j also revealed gradually improved interfacial charge transfer and extraction in the order of the control (1.99 µs), KCl (1.90 µs), KMS (1.36 µs), KTFSI (0.82 µs), and KFSI (0.30 µs) based devices. The transient photovoltage (TPV) results as shown in Fig. 4k demonstrated that the carrier decay lifetime of the control device (9.59 µs) was increased to 9.99, 21.42, 22.20 and 23.07 µs for KCl, KMS, KTFSI, and KFSI modified devices, respectively, suggesting nonradiative recombination was

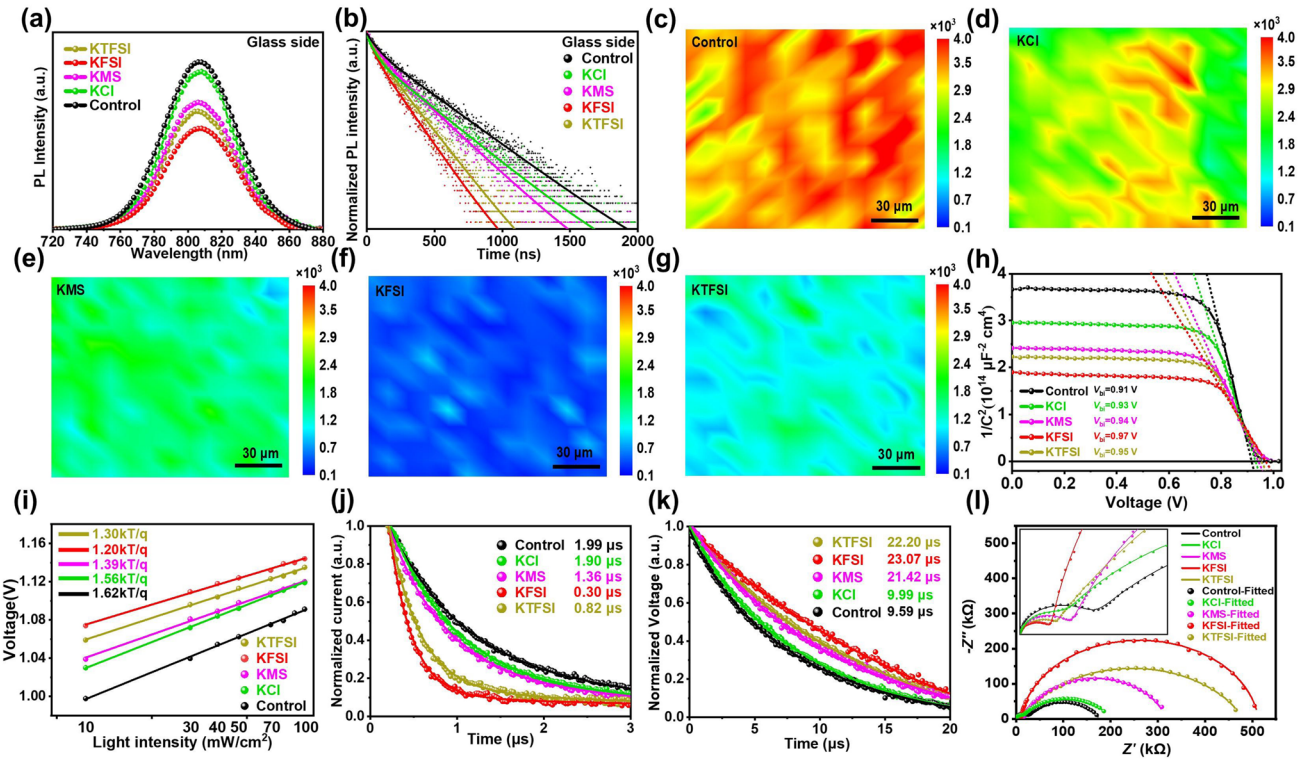

Fig. 4 **a** SSPL and **b** TRPL spectra of the perovskite films deposited on SnO_2 films without and with modifiers. PL mapping images of the perovskite films prepared on the **c** bare SnO_2 and SnO_2 modified by **d** KCl, **e** KMS, **f** KFSI and **g** KTFSI. **h** Mott–Schottky analysis, **i** TPC, **j** TPV and **k** V_{OC} as a function of light intensities for the control and modified PSCs. **l** Nyquist plots of the control and modified devices measured at a bias of 0.8 V in the frequency range of 1 MHz to 0.01 Hz in the dark. An enlarged view of the high-frequency region is shown in the inset

suppressed owing to effective defect passivation, ameliorative band alignment and enhanced perovskite crystallization. The V_{OC} was plotted as a function of light intensity in Fig. 4i. The ideal factor (n) was calculated by Eq. (6) of fitting straight line:

$$\text{slope} = \text{nkT}/q \tag{6}$$

where k stands for the Boltzmann constant, T represents the absolute temperature, and q denotes the elementary charge. Compared with the control device (1.62), the devices with KCl, KMS, KTFSI and KFSI realized lower n values of 1.56, 1.39, 1.30 and 1.20, respectively, which is indicative of memorably restrained non-radiative recombination, agreeing with the above TPV results. The exponential relationship between J_{SC} and light intensity is also shown in Fig. S17 and the exponential factor α of the KFSI modified device (0.979) was highest, followed by the device with KTFSI (0.968), the device with KMS (0.956), the device with KCl (0.950), and the control device (0.948). This indicates that KFSI modified device showed efficient carrier transport and extraction.

Electrochemical impedance spectroscopy (EIS) measurement was performed to explore the underlying mechanism of charge transfer and recombination in PSCs (Figs. 4l and S18). The decrease in charge transfer resistance (R_{ct}) values in the high frequency region and the increase in carrier recombination resistance (R_{rec}) in the low frequency region indicate that the nonradiative recombination was suppressed and interfacial charge transfer was promoted after interface modification. The improved interfacial energy band alignment mainly contributed to ameliorated interfacial carrier extraction and transfer. The reduced interfacial defects, reduced grain boundary density, increased crystallinity and improved crystal plane orientation should be primarily responsible for inhibited carrier nonradiative recombination.

3.5 Photovoltaic Performance

The photovoltaic performance of the planar PSCs modified by various concentrations of modifiers based on two step method were compared (Figs. S19–S22 and Tables S5–S8). Obviously, it can be found in Figs. S22 and 5a that increased PCE was ascribed to simultaneous enhancement of V_{OC}, short-circuit current density (J_{SC}) and FF. Improved V_{OC} and FF should be put down to reduced defect density of perovskite layer and ETL, increased carrier lifetimes, ameliorated perovskite crystallization and suppressed interfacial nonradiative recombination. Among all modifiers, KFSI-modified device exhibited the best photovoltaic performance. All potassium salts containing non-halogen anions are better in device performance with respect to KCl and reference device. This indicates that non-halogen anions could be very promising in defect passivation and crystallization enhancement than halide anions in consideration of structure tunability of the former. Figure 5b exhibits J-V curves of the best-performing PSCs without and with KCl, KMS, KFSI and KTFSI. Compared with the control device (a J_{SC} of 24.50 mA cm^{-2}, a V_{OC} of 1.114 V, an FF of 0.789 and PCE of 21.20%), the KCl-modified device showed a slightly enhanced PCE of 21.38% (a J_{SC} of 24.58 mA cm^{-2}, a V_{OC} of 1.119 V, and an FF of 0.790). In contrast, the devices based on potassium salts with non-halogen anions exhibited obvious PCE enhancement. The KMS, KTFSI and KFSI modified devices achieved a PCE of 22.02% (a J_{SC} of 24.68 mA cm^{-2}, a V_{OC} of 1.121 V, and an FF of 0.804), a PCE of 22.23% (a J_{SC} of 24.77 mA cm^{-2}, a V_{OC} of 1.139 V, and an FF of 0.809), and a PCE of 23.21% (a J_{SC} of 25.12 mA cm^{-2}, a V_{OC} of 1.148 V, and an FF of 0.817), respectively. This suggests that it is of critical importance to incorporate F and S=O functional groups to enhance chemical interaction between non-halogen anions and interface. As illustrated in Fig. 5c, the integrated current densities of the control, KCl, KMS, KTFSI and KFSI modified devices were 23.03, 23.07, 23.30, 23.82 and 24.34 mA cm^{-2}, respectively. It is revealed in Fig. 5d–e that steady-state current densities and PCEs of the control, KCl, KMS, KTFSI and KFSI modified devices after 300 s were 21.06 mA cm^{-2} and 20.43%, 21.23 mA cm^{-2} and 20.85%, 21.64 mA cm^{-2} and 21.54%, 22.30 mA cm^{-2} and 21.97%, and 23.02 mA cm^{-2} and 22.86%, respectively. The KFSI-modified PSC with PEAI post treatment delivered a further improved PCE of 24.17% in reverse scan and 24.04% in forward scan (Fig. 5f and Table S9).

Finally, we investigated the stability of the unencapsulated control and modified devices. Figure 5g shows the moisture stability of the control and modified devices under a relative humidity of 30% – 35% at 25 °C. After 2264 h, the control device degraded to 78% of its initial value whereas the KCl, KMS, KTFSI and KFSI-modified devices degraded to 86%, 88%, 91% and 94% of their initial PCEs, respectively, which is indicative of improved moisture stability after interface modification. The thermal stability was evaluated by aging

 https://doi.org/10.1007/s40820-022-00992-5

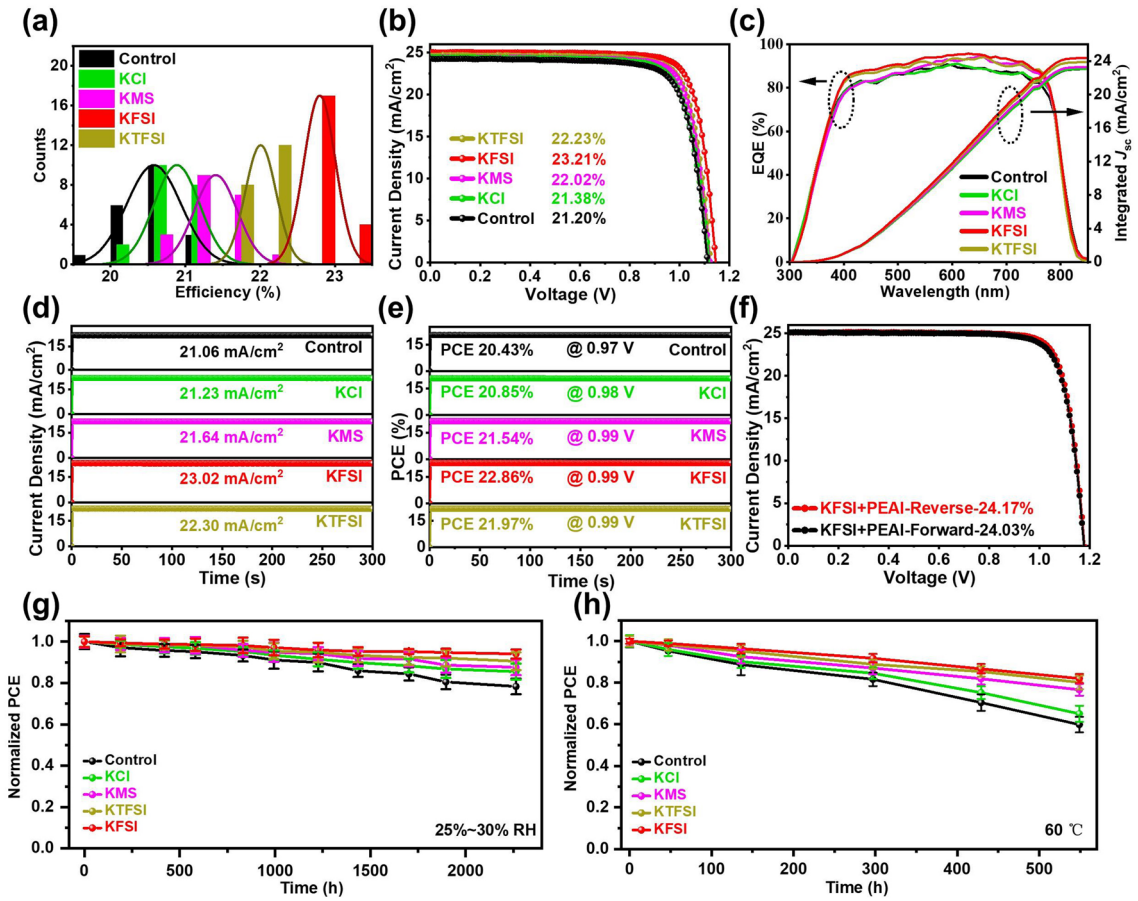

Fig. 5 **a** Statistical distribution of the PCEs of the PSCs based on the SnO_2 films without and with KCl, KMS, KTFSI and KFSI. The statistical data were obtained from 20 individual cells for each kind of device. **b** *J–V* curves and **c** EQE spectra of the best-performing devices based on bare SnO_2 film and KCl, KMS, KTFSI and KFSI modified SnO_2 films. *J–V* curves were measured under simulated AM 1.5G one sun illumination of 100 mW cm^{-2}. **d** Steady-state current density and **e** PCE versus time for the best-performing devices employing pristine and modified SnO_2 films measured at the maximum power point. **f** *J-V* curves of the KFSI-modified champion PSCs with PEAI posttreatment. PCE evolution of the unencapsulated control and modified **g** under 25%-30% relative humidity at room temperature in the dark, **h** at 60 °C in the dark in the nitrogen-filled glovebox. Error bars represent the standard deviation of five devices

unencapsulated devices at 60 °C in a nitrogen-filled glove box (Fig. 5h). After aging for 549 h, it was found that the KCl, KMS, KTFSI and KFSI-modified devices maintained 65%, 77%, 80% and 82% of their initial PCEs while only 60% for the control device, respectively, indicating that thermal stability was improved after interface modification. Figure 5i exhibit the photostability of the control and modified devices under one sun illumination at room temperature, where the devices were located in the glovebox filled with nitrogen. After 343 h, the control device degraded to 66% of its initial value whereas the KCl, KMS, KTFSI and KFSI-modified devices degraded to 72%, 74.7%, 78% and 85% of their initial PCEs, respectively, which is indicative of improved photostability after interface modification (Fig. S24).

The trap-assisted nonradiative recombination is one of main reasons for device degradation [52]. Therefore, the effective passivation of modifiers for the defects from perovskite and SnO_2 films should be mainly responsible for improved device stability. In addition, improved interfacial contact by chemically bridging perovskite layer and ETL should be another important origin of enhanced stability [17, 27, 28]. In short, our interfacial modification strategy can enhance efficiency and stability simultaneously.

4 Conclusions

In summary, we developed a buried interface stabilization strategy based on synergistic engineering of fluorine and sulfonyl functional groups. A series of potassium salts (KCl, KMS, KFSI and KTFSI) were used to modify SnO_2/perovskite buried interface. Multiple chemical bonds were realized by simultaneous introduction of F and S=O. First, F can form hydrogen bond with organic cations and form coordination bond with Pb^{2+} and Sn^{4+}. Second, S=O functional group and non-halogen anion can form coordination bond with Pb^{2+} and Sn^{4+}. Finally, K^+ and non-halogen anions can form ionic bonds with cation and halide vacancy defects, respectively. The crystallization kinetics was regulated through the compromise between chemical interaction strength and wettability of substrates. The introduction of F would enhance chemical interaction while it also would increase hydrophobicity of surface of ETL. Appropriate hydrophobicity is conducive to suppressing heterogeneous nucleation and thus promoting perovskite crystallization but too high hydrophobicity hinders perovskite crystallization. The KFSI-modified device obtained an appealing PCE of 24.17% along with excellent stability. This work demonstrated great potentials of non-halogen anions and provide a feasible and effective approach toward managing interfacial carrier via the synergistic design of organic functional groups.

Acknowledgments This work is financially supported by the Defense Industrial Technology Development Program (JCKY2017110C0654), National Natural Science Foundation of China (11974063, 61904023, 62274018), Chongqing Special Postdoctoral Science Foundation (cstc2019jcyj-bsh0026) and Fundamental Research Funds for the Central Universities (2021CDJQY-022). We would like to thank the Analytical and Testing Center of Chongqing University for various measurements. We also thank Beijing Synchrotron Radiation Facility (BSRF) for GIWAX measurement.

Funding Open access funding provided by Shanghai Jiao Tong University.

Supplementary Information The online version contains supplementary material available at https://doi.org/10.1007/s40820-022-00992-5.

References

1. X. Li, W. Zhang, X. Guo, C. Lu, J. Wei et al., Constructing heterojunctions by surface sulfidation for efficient inverted perovskite solar cells. Science **375**(6579), 434–437 (2022). https://doi.org/10.1126/science.abl5676
2. T. Zhou, M. Wang, Z. Zang, L. Fang, Stable dynamics performance and high efficiency of ABX_3-type super-alkali perovskites first obtained by introducing H_5O_2 cation. Adv. Energy Mater. **9**(29), 1900664 (2019). https://doi.org/10.1002/aenm.201900664
3. R. Yuan, B. Cai, Y. Lv, X. Gao, J. Gu et al., Boosted charge extraction of NbO_x-enveloped SnO_2 nanocrystals enables 24% efficient planar perovskite solar cells. Energy Environ. Sci. **14**, 5074–5083 (2021). https://doi.org/10.1039/D1EE01519B
4. M. Kim, J. Jeong, H. Lu, T.K. Lee, F.T. Eickemeyer et al., Conformal quantum dot SnO_2 layers as electron transporters for efficient perovskite solar cells. Science **375**(6578), 302–306 (2022). https://doi.org/10.1126/science.abh1885
5. M. Li, H. Li, Q. Zhuang, D. He, B. Liu et al., Stabilizing perovskite precursor by synergy of functional groups for NiOx-based inverted solar cells with 23.5% efficiency. Angew. Chem. Int. Ed. (2022). https://doi.org/10.1002/anie.202206914
6. A. Kojima, K. Teshima, Y. Shirai, T. Miyasaka, Organometal halide perovskites as visible-light sensitizers for photovoltaic cells. J. Am. Chem. Soc. **131**(17), 6050–6051 (2009). https://doi.org/10.1021/ja809598r
7. NREL, Best research-cell efficiency chart. https://www.nrel.gov/pv/cell-efficiency.html
8. J. Chen, N.G. Park, Materials and methods for interface engineering toward stable and efficient perovskite solar cells. ACS Energy Lett. **5**(8), 2742–2786 (2020). https://doi.org/10.1021/acsenergylett.0c01240
9. J. Deng, H. Zhang, K. Wei, Y. Xiao, C. Zhang et al., Molecular bridge assisted bifacial defect healing enables low energy loss for efficient and stable perovskite solar cells. Adv. Funct. Mater. (2022). https://doi.org/10.1002/adfm.202209516
10. Z.W. Gao, Y. Wang, W.C.H. Choy, Buried interface modification in perovskite solar cells: a materials perspective. Adv.

Energy Mater. **12**(20), 2104030 (2022). https://doi.org/10.1002/aenm.202104030

11. Z. Ni, C. Bao, Y. Liu, Q. Jiang, W.Q. Wu et al., Resolving spatial and energetic distributions of trap states in metal halide perovskite solar cells. Science **367**(6484), 1352–1358 (2020). https://doi.org/10.1126/science.aba0893
12. X. Zuo, B. Kim, B. Liu, D. He, L. Bai et al., Passivating buried interface via self-assembled novel sulfonium salt toward stable and efficient perovskite solar cells. Chem. Eng. J. **431**, 133209 (2022). https://doi.org/10.1016/j.cej.2021.133209
13. B. Chen, P.N. Rudd, S. Yang, Y. Yuan, J. Huang, Imperfections and their passivation in halide perovskite solar cells. Chem. Soc Rev. **48**, 3842–3867 (2019). https://doi.org/10.1039/C8CS00853A
14. S.Y. Park, K. Zhu, Advances in SnO_2 for efficient and stable n–i–p perovskite solar cells. Adv. Mater. **34**(27), 2110438 (2022). https://doi.org/10.1002/adma.202110438
15. Ç. Kılıç, A. Zunger, Origins of coexistence of conductivity and transparency in SnO_2. Phys. Rev. Lett. **88**, 095501 (2002). https://doi.org/10.1103/PhysRevLett.88.095501
16. Y. Dong, W. Shen, W. Dong, C. Bai, J. Zhao et al., Chlorobenzenesulfonic potassium salts as the efficient multifunctional passivator for the buried interface in regular perovskite solar cells. Adv. Energy Mater. **12**(20), 2200417 (2022). https://doi.org/10.1002/aenm.202200417
17. D. Gao, L. Yang, X. Ma, X. Shang, C. Wang et al., Passivating buried interface with multifunctional novel ionic liquid containing simultaneously fluorinated anion and cation yielding stable perovskite solar cells over 23% efficiency. J. Energy Chem. **69**, 659–666 (2022). https://doi.org/10.1016/j.jechem.2022.02.016
18. Z. Xiong, X. Chen, B. Zhang, G.O. Odunmbaku, Z. Ou et al., Simultaneous interfacial modification and crystallization control by biguanide hydrochloride for stable perovskite solar cells with PCE of 24.4%. Adv. Mater. **34**(8), 2106118 (2022). https://doi.org/10.1002/adma.202106118
19. F. Ye, J. Ma, C. Chen, H. Wang, Y. Xu et al., Roles of macl in sequentially deposited bromine-free perovskite absorbers for efficient solar cells. Adv. Mater. **33**(3), 2007126 (2021). https://doi.org/10.1002/adma.202007126
20. Q. Jiang, Y. Zhao, X. Zhang, X. Yang, Y. Chen et al., Surface passivation of perovskite film for efficient solar cells. Nat. Photonics **13**, 460–466 (2019). https://doi.org/10.1038/s41566-019-0398-2
21. H. Min, D.Y. Lee, J. Kim, G. Kim, K.S. Lee et al., Perovskite solar cells with atomically coherent interlayers on SnO_2 electrodes. Nature **598**, 444–450 (2021). https://doi.org/10.1038/s41586-021-03964-8
22. H. Bi, X. Zuo, B. Liu, D. He, L. Bai et al., Multifunctional organic ammonium salt-modified SnO_2 nanoparticles toward efficient and stable planar perovskite solar cells. J. Mater. Chem. A **9**(7), 3940–3951 (2021). https://doi.org/10.1039/D0TA12612H
23. S. You, H. Zeng, Z. Ku, X. Wang, Z. Wang et al., Multifunctional polymer-regulated SnO_2 nanocrystals enhance interface contact for efficient and stable planar perovskite solar cells. Adv. Mater. **32**(43), 2003990 (2020). https://doi.org/10.1002/adma.202003990
24. I. Levine, A. Al-Ashouri, A. Musiienko, H. Hempel, A. Magomedov et al., Charge transfer rates and electron trapping at buried interfaces of perovskite solar cells. Joule **5**, 2915–2933 (2021). https://doi.org/10.1016/j.joule.2021.07.016
25. E.H. Jung, B. Chen, K. Bertens, M. Vafaie, S. Teale et al., Bifunctional surface engineering on SnO_2 reduces energy loss in perovskite solar cells. ACS Energy Lett. **5**(9), 2796–2801 (2020). https://doi.org/10.1021/acsenergylett.0c01566
26. K. Choi, J. Lee, H.I. Kim, C.W. Park, G.W. Kim et al., Thermally stable, planar hybrid perovskite solar cells with high efficiency. Energy Environ. Sci. **11**(11), 3238–3247 (2018). https://doi.org/10.1039/C8EE02242A
27. J. Chen, X. Zhao, S.G. Kim, N.G. Park, Multifunctional chemical linker imidazoleacetic acid hydrochloride for 21% efficient and stable planar perovskite solar cells. Adv. Mater. **31**(39), 1902902 (2019). https://doi.org/10.1002/adma.201902902
28. H. Bi, B. Liu, D. He, L. Bai, W. Wang et al., Interfacial defect passivation and stress release by multifunctional KPF_6 modification for planar perovskite solar cells with enhanced efficiency and stability. Chem. Eng. J. **418**, 129375 (2021). https://doi.org/10.1016/j.cej.2021.129375
29. L. Zhu, X. Zhang, M. Li, X. Shang, K. Lei et al., Trap state passivation by rational ligand molecule engineering toward efficient and stable perovskite solar cells exceeding 23% efficiency. Adv. Energy Mater. **11**(20), 2100529 (2021). https://doi.org/10.1002/aenm.202100529
30. Z. Zhang, J. Liang, J. Wang, Y. Zheng, X. Wu et al., Resolving mixed intermediate phases in methylammonium-free Sn-Pb alloyed perovskites for high-performance solar cells. Nano-Micro Lett. **14**, 165 (2022). https://doi.org/10.1007/s40820-022-00918-1
31. D. Bi, X. Li, J.V. Milic, D.J. Kubicki, N. Pellet et al., Multifunctional molecular modulators for perovskite solar cells with over 20% efficiency and high operational stability. Nat. Commun. **9**, 4482 (2018). https://doi.org/10.1038/s41467-018-06709-w
32. B. Liu, H. Bi, D. He, L. Bai, W. Wang et al., Interfacial defect passivation and stress release via multi-active-site ligand anchoring enables efficient and stable methylammonium-free perovskite solar cells. ACS Energy Lett. **6**(7), 2526–2538 (2021). https://doi.org/10.1021/acsenergylett.1c00794
33. J. Chen, N.G. Park, Nonhalide materials for efficient and stable perovskite solar cells. Small Method. **5**(6), 2100311 (2021). https://doi.org/10.1002/smtd.202100311
34. F.K. Aldibaja, L. Badia, E. Mas-Marzá, R.S. Sánchez, E.M. Barea et al., Effect of different lead precursors on perovskite solar cell performance and stability. J. Mater. Chem. A **3**(17), 9194–9200 (2015). https://doi.org/10.1039/C4TA06198E
35. E. Jiang, Y. Ai, J. Yan, N. Li, L. Lin et al., Phosphate-passivated SnO_2 electron transport layer for high-performance perovskite solar cells. ACS Appl. Mater. Interface. **11**(40), 36727–36734 (2019). https://doi.org/10.1021/acsami.9b11817

36. J. Dagar, K. Hirselandt, A. Merdasa, A. Czudek, R. Munir et al., Alkali salts as interface modifiers in n-i-p hybrid perovskite solar cells. Sol. RRL **3**, 1900088 (2019). https://doi.org/10.1002/solr.201900088
37. J. Jeong, M. Kim, J. Seo, H. Lu, P. Ahlawat et al., Pseudo-halide anion engineering for α-$FAPbI_3$ perovskite solar cells. Nature **592**, 381–385 (2021). https://doi.org/10.1038/s41586-021-03406-5
38. W. Wang, Q. Zhou, D. He, B. Liu, L. Bai et al., Self-formed multifunctional grain boundary passivation layer achieving 22.4% efficient and stable perovskite solar cells. Sol. RRL **6**, 2100893 (2022). https://doi.org/10.1002/solr.202100893
39. C. Zhang, H. Wang, H. Li, Q. Zhuang, C. Gong et al., Simultaneous passivation of bulk and interface defects through synergistic effect of anion and cation toward efficient and stable planar perovskite solar cells. J. Energy Chem. **63**, 452–460 (2021). https://doi.org/10.1016/j.jechem.2021.07.011
40. S. Yuan, Y. Cai, S. Yang, H. Zhao, F. Qian et al., Simultaneous cesium and acetate coalloying improves efficiency and stability of $FA_{0.85}MA_{0.15}$PbI3 perovskite solar cell with an efficiency of 21.95%. Sol. RRL **3**, 190 (2019). https://doi.org/10.1002/solr.201900220
41. Q. Han, Y. Bai, J. Liu, K.Z. Du, T. Li et al., Additive engineering for high-performance room-temperature-processed perovskite absorbers with micron-size grains and microsecond-range carrier lifetimes. Energy Environ. Sci. **10**, 2365–2371 (2017). https://doi.org/10.1039/C7EE02272G
42. D. He, T. Zhou, B. Liu, L. Bai, W. Wang et al., Interfacial defect passivation by novel phosphonium salts yields 22% efficiency perovskite solar cells: experimental and theoretical evidence. EcoMat **4**, e12158 (2022). https://doi.org/10.1002/eom2.12158
43. T. Singh, S. Öz, A. Sasinska, R. Frohnhoven, S. Mathur et al., Sulfate-assisted interfacial engineering for high yield and efficiency of triple cation perovskite solar cells with alkali-doped TiO_2 electron-transporting layers. Adv. Funct. Mater. **28**(14), 1706287 (2018). https://doi.org/10.1002/adfm.201706287
44. Q. Chen, G. Zhai, J. Ren, Y. Huo, Z. Yun et al., Surface passivation of perovskite films by potassium bis(fluorosulfonyl) imide for efficient solar cells. Org. Electron. **107**, 106544 (2022). https://doi.org/10.1016/j.orgel.2022.106544
45. Q. Zhuang, H. Wang, C. Zhang, C. Gong, H. Li et al., Ion diffusion-induced double layer doping toward stable and efficient perovskite solar cells. Nano Res. **15**, 5114–5122 (2022). https://doi.org/10.1007/s12274-022-4135-7
46. W. Dong, W. Qiao, S. Xiong, J. Yang, X. Wang et al., Surface passivation and energetic modification suppress nonradiative recombination in perovskite solar cells. Nano-Micro Lett. **14**, 108 (2022). https://doi.org/10.1007/s40820-022-00854-0
47. D.H. Kim, J. Park, Z. Li, M. Yang, J.S. Park et al., 300% enhancement of carrier mobility in uniaxial-oriented perovskite films formed by topotactic-oriented attachment. Adv. Mater. **29**(23), 1606831 (2017). https://doi.org/10.1002/adma.201606831
48. C.C. Stoumpos, C.D. Malliakas, M.G. Kanatzidis, Semiconducting tin and lead iodide perovskites with organic cations: phase transitions, high mobilities, and near-infrared photoluminescent properties. Inorg. Chem. **52**, 9019–9038 (2013). https://doi.org/10.1021/ic401215x
49. C. Bi, Q. Wang, Y. Shao, Y. Yuan, Z. Xiao et al., Non-wetting surface-driven high-aspect-ratio crystalline grain growth for efficient hybrid perovskite solar cells. Nat. Commun. **6**, 7747 (2015). https://doi.org/10.1038/ncomms8747
50. Q. Jiang, Z. Chu, P. Wang, X. Yang, H. Liu et al., Planar-structure perovskite solar cells with efficiency beyond 21. Adv. Mater. **29**(46), 1703852 (2017). https://doi.org/10.1002/adma.201703852
51. Z. Xu, Z. Liu, N. Li, G. Tang, G. Zheng et al., A thermodynamically favored crystal orientation in mixed formamidinium/methylammonium perovskite for efficient solar cells. Adv. Mater. **31**(24), 1900390 (2019). https://doi.org/10.1002/adma.201900390
52. J. Xu, J. Cui, S. Yang, Y. Han, X. Guo et al., Unraveling passivation mechanism of imidazolium-based ionic liquids on inorganic perovskite to achieve near-record-efficiency $CsPbI_2Br$ solar cells. Nano-Micro Lett. **14**, 7 (2021). https://doi.org/10.1007/s40820-021-00763-8

 https://doi.org/10.1007/s40820-022-00992-5